



HAL
open science

Unraveling the Role of Alkali Cations in the Growth Mechanism of Gd₂O₂S Nanoparticles

Clément Larquet, David Carriere, Anh-Minh Nguyen, Thi Kim-Chi Le, Xavier Frogneux-Plé, Isabelle Génois, Patrick Le Griel, Andrea Gauzzi, Clément Sanchez, Sophie Carencó

► To cite this version:

Clément Larquet, David Carriere, Anh-Minh Nguyen, Thi Kim-Chi Le, Xavier Frogneux-Plé, et al.. Unraveling the Role of Alkali Cations in the Growth Mechanism of Gd₂O₂S Nanoparticles. *Chemistry of Materials*, In press, 32, pp.1131-1139. 10.1021/acs.chemmater.9b04059 . cea-02440126

HAL Id: cea-02440126

<https://cea.hal.science/cea-02440126>

Submitted on 15 Jan 2020

HAL is a multi-disciplinary open access archive for the deposit and dissemination of scientific research documents, whether they are published or not. The documents may come from teaching and research institutions in France or abroad, or from public or private research centers.

L'archive ouverte pluridisciplinaire **HAL**, est destinée au dépôt et à la diffusion de documents scientifiques de niveau recherche, publiés ou non, émanant des établissements d'enseignement et de recherche français ou étrangers, des laboratoires publics ou privés.

Unraveling the Role of Alkali Cations in the Growth Mechanism of Gd₂O₂S Nanoparticles

Clément Larquet,^{1,2} David Carriere,³ Anh-Minh Nguyen,¹ Thi Kim-Chi Le,¹ Xavier Frogneux-Plé,¹ Isabelle Génois,¹ Patrick Le Griel,¹ Andrea Gauzzi,² Clément Sanchez,¹ Sophie Carencó^{1,}*

¹ Sorbonne Université, CNRS, Collège de France, Laboratoire de Chimie de la Matière Condensée de Paris, 4 place Jussieu, 75005 Paris, France

² Sorbonne Université, Institut de Minéralogie de Physique des Matériaux et de Cosmologie, CNRS, 4, place Jussieu, 75005 Paris, France

³ LIONS, NIMBE, CEA, CNRS, Université Paris-Saclay, CEA Saclay 91191 Gif sur Yvette Cedex

* Corresponding author e-mail: sophie.carenco@sorbonne-universite.fr

Abstract:

Alkali cations are required for the colloidal synthesis of $\text{Ln}_2\text{O}_2\text{S}$ nanoplates in organic solvent. Based on a thorough experimental analysis using various lanthanides and three alkali ions, we challenge the commonly accepted scenario of partial lanthanide substitution by the alkali, which is supposed to favor the sulfide insertion over the oxide one. Using SAXS-WAXS on aliquots taken from the synthesis medium, we demonstrate the formation of an alkali-stabilized oleate mesophase acting as a template for nanoparticles nucleation and growth. As a consequence, the alkali is not incorporated into the crystalline structure; nanoparticle growth requires only a low alkali concentration that can be readily washed away from the final nanoparticles powder. We expect that similar mesophases may form in other colloidal synthesis using oleates and small cations.

1. Introduction

While lanthanide oxysulfides in bulk form have been readily employed in a number of applications like screens, lasers and scintillators, their preparation in nanoparticle form has been reported for the first time only in 2000.¹ The reason of this delay is the limited stability of oxysulfide nanoparticles due to competing oxide or sulfide phases. The development of a general and robust synthesis route of these nanoparticles would therefore be important to drive LED nanotechnology towards new directions. A further emerging field of application of oxysulfide nanoparticles is nanomedicine, where doped $\text{Gd}_2\text{O}_2\text{S}$ is being investigated as a multifunctional luminescent vector for diagnosis and contrast agent in MRI^{2,3}, which requires a reproducible and versatile preparation route of mono and bicationic $\text{Ln}_2\text{O}_2\text{S}$ nanoparticles.

In earlier reports, lanthanide oxysulfides nanoparticles were prepared with irregular sizes and morphologies and the sulfide content was poorly controlled. A major advance was made in 2011 by Ding *et al.*⁴ who synthesized ultrasmall $\text{Ln}_2\text{O}_2\text{S}$ nanoplates by employing a

straightforward and versatile protocol for Ln = La, Pr, Nd, Sm, Eu, Gd, Tb, as well as for Y. The authors highlighted the crucial role played by an alkaline cation in the formation of crystalline nanoparticles. For all lanthanide compounds investigated, sodium acetylacetonate (Na(acac)) was systematically added in the reaction medium.⁴ During the reaction, Ln₂O₂S formation competes with Ln₂O₃ rather than Ln₂S₃, because of the strong affinity of lanthanides with oxygen. The authors proposed that Na^I substitutes Ln^{III} in the crystal lattice during growth and that this substitution creates more oxygen vacancies than sulfur vacancies, which favors the formation of the sulfide rather than the oxide. The final structure was described as Na-doped Ln₂O₂S nanoplates, containing *ca.* 25% Na *vs.* Ln. Surprisingly, X-ray diffraction (XRD) on powders gives no indication of any alteration of the Ln₂O₂S structure by Na doping. In addition, small Y₂O₂S nanoparticles ($\varnothing < 5$ nm) were prepared using Li(acac) instead of Na(acac).⁴

In 2013, the same group reported that the substitution of the lanthanide ion with other alkaline ions (lithium and potassium) is effective in the synthesis of La₂O₂S nanoparticles.⁵ In the case of Na and K substitution, the authors obtained well-crystallized thin nanoplates of 23 and 45 nm size, respectively, while Li substitution led to the formation of smaller (9 nm-wide) and poorly crystallized nanoplates. They also found that K is effective in the crystallization of other Eu, Gd and Yb oxysulfide nanoparticles. As in the previous work, *ab initio* calculations suggest that oxygen vacancies are more stable than sulfur ones when alkaline ions are present in the structure, which explains the formation of Ln₂O₂S nanoparticles. The authors also noticed that nanoparticles prepared with Li and K contain less sulfur than those prepared with Na.

These two seminal articles raise a series of questions. First, the substitution of a significant amount of trivalent lanthanide ions by monovalent ones is expected to distort the lattice owing to the different cation size (see Figure S1). Note that, in the final product, the substitution

level is at least 6 - 7 % for K and up to 25 % for Na, while it could not be measured by means of EDS in the case of Li. Some of us reported that a distortion does indeed occur even for substitutions of cations with comparable size, *i.e.* Ce/Gd, with $r = 1.21$ and 1.14 \AA , respectively, as indicated by a shift of XRD Bragg peaks (see a typical XRD pattern of $\text{Gd}_2\text{O}_2\text{S}$ in Figure S2).⁶ Therefore, one expects much larger distortions in the above case of K/La or Li/La substitutions, owing to the much larger difference in cation size, with $r(\text{K}^{\text{I}}(\text{VII})) = 1.60 \text{ \AA}$, $r(\text{Li}^{\text{I}}(\text{VII})) \approx 1 \text{ \AA}$, $r(\text{La}(\text{VII})) = 1.24 \text{ \AA}$. So, if the crystallization process was driven by the substitution of the lanthanide ion, as suggested by the authors, one would expect a better crystallization of the $\text{La}_2\text{O}_2\text{S}$ particles in the case of Na- rather than K-substitution, for the former ion is smaller ($r(\text{Na}^{\text{I}}(\text{VII})) = 1.26 \text{ \AA}$) and the substitution is energetically more favorable. In fact, the opposite result was found, thus raising a doubt regarding the validity of the above suggestion.

Second, the lack of sulfur upon Li or K substitution remains to be explained. The electronegativity of Li, K and Na are close ($\chi_{\text{Li}} = 0.98$, $\chi_{\text{K}} = 0.82$ and $\chi_{\text{Na}} = 0.93$ on Pauling scale), hence their relative affinity with sulfur and oxygen should also be close. One possible explanation is that the nanoparticles are terminated by $[\text{Ln}_2\text{O}_2]^{2+}$ planes stabilized by oleates⁷. However, this argument would suggest that the K-substituted nanoparticles reported by Ding *et al.* exhibit higher sulfur content than the Li-substituted ones, for the former are larger and the surface/volume ratio is smaller, while the opposite is found experimentally.

In view of the above considerations, it appears that the alkali ion plays a complex role in the formation of $\text{Ln}_2\text{O}_2\text{S}$ nanoplates, which remains to be understood. Available data point at an apparently inconsistent behavior of crystal quality and of oxygen *vs.* sulfur stoichiometry with the nature of the alkali ion. In order to explain this inconsistency, we should put into question the current hypothesis that the alkali ions remain in the nanoplates crystal lattice. To do so, in the present study, we first examine the influence of the cation nature on nanoparticles

formation. Second, our analysis of X-ray scattering data suggests an alternative model for nanoparticles nucleation and growth. We demonstrate that the primary role of the alkali cation is to form a lamellar mesophase into which the nanoparticles nucleate without entering into the final crystal structure of the nanoparticles.

2. Results and discussion

2.1 Sodium content in the nanoparticles powders

Bicationic metal oxysulfide nanoparticles containing Gd and Ce of general formula $\text{Gd}_{2(1-y)}\text{Ce}_{2y}\text{O}_2\text{S}$ were prepared following a protocol previously described.⁶ Briefly, $\text{Gd}(\text{acac})_3 \cdot n\text{H}_2\text{O}$ (0.5 mmol) and $\text{Ce}(\text{acac})_3 \cdot n\text{H}_2\text{O}$, elemental sulfur S_8 (0.5 equiv. S vs. the metals) and Na(oleate) (1 equiv. vs. Gd) were mixed in degassed oleylamine, oleic acid and 1-octadecene. The reaction was conducted at 310 °C for 30 minutes and yielded nanoparticles similar to those presented in a previous study⁶ and in Figure S2 ($y = 0\%$). These nanoparticles were isolated by centrifugation and washed at least three times using a THF/ethanol (1/5 in volume) mixture.

In agreement with Ding *et al.*,⁴ we observed that Na remained in the powder of $\text{Gd}_{2(1-y)}\text{Ce}_{2y}\text{O}_2\text{S}$ nanoparticles. A series of EDS results obtained in several experiments are presented in Figure 1A for different y values. Note the scattering of the values of Na concentration within the 5 - 40 % range and that no clear trend emerges. The Na content is never lower than 5 %, *i.e.* 0.05 equiv. vs. the metals. These scattered values are attributed to the limited reproducibility of the washing step. Indeed, the washing efficiency is related to the quality of the colloidal dispersion made by sonication and vortex stirring between each step and both parameters typically vary from sample to sample even when using the same solvent volume. Since colloidal stability is related to surface accessibility, we put forward the

hypothesis that Na is mainly located at the surface of the nanoparticles and weakly bonded to them.

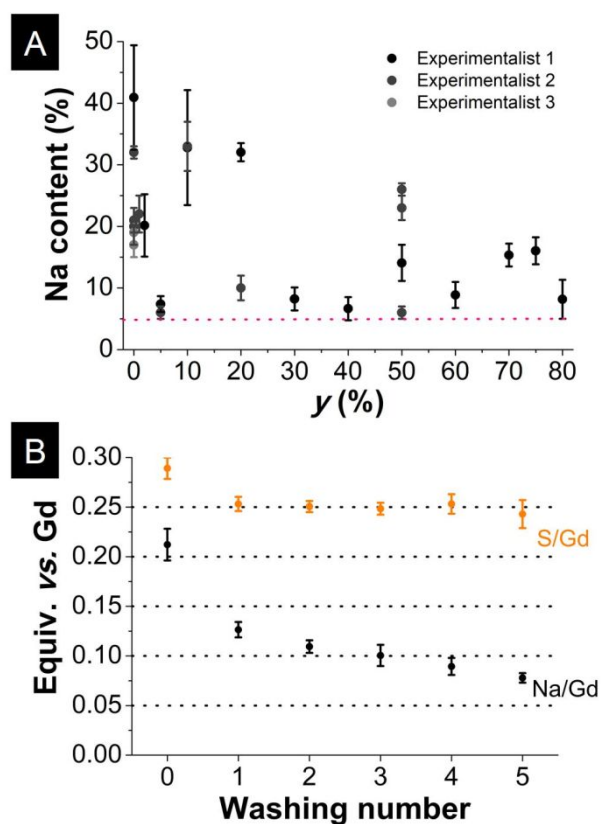


Figure 1: (A) Na content of $Gd_{2(1-y)}Ce_{2y}O_2S$ nanoparticles, isolated and washed under similar conditions, as a function of the Gd/Ce substitution level, y . The sodium content in percent is defined as $Na(\%) = n_{Na} / (n_{Gd} + n_{Ce})$. (B) Evolution of Na and S compositions normalized to Gd during the washing process of Gd_2O_2S nanoplates. The values indicate the average EDS composition measured on 5 different regions of each sample. Washing “0” refers to the powder centrifuged from the crude solution, with ethanol only (separation step).

In order to investigate this hypothesis, the Na content was monitored at each step of the washing process. We also monitored the S content, to ensure that sulfur enters the nanoparticles rather than being trapped in the precipitate. Typically, the particles are precipitated from the reaction mixture upon addition of ethanol and then washed several times with a mixture THF/ethanol 1/5 in volume, a process similar to that described by Ding *et al.*⁴

Figure 1B indicates the Na/Gd and S/Gd ratio. We observed that the first precipitate, obtained by adding ethanol, already contains less Na (0.21 equiv. vs. Gd) than the powders introduced in the reaction medium (1 equiv.). The first washing step removed an additional 0.08 equiv. vs. Gd. During the following washing steps, the Na concentration was found to monotonously decrease from 0.13 equiv. to 0.08 equiv. vs. Gd. The removal of most of the initial Na during the washing is in agreement with our hypothesis that Na is weakly bonded to the nanoparticles. The fact that the removal process is slow and incomplete is attributed to the limited solubility of Na cations in the THF/ethanol mixture. In comparison, the sulfur concentration does not change upon washing, which is consistent with the fact that sulfur is required to form the nanoparticle structure. Moreover, the absence of sodium doping in the structure was recently confirmed from a direct structural analysis by pair-distribution function (PDF): fitting of the experimental data with a model of Gd₂O₂S nanoparticles without Na doping led to excellent agreement.⁸

In conclusion, the above results suggest that Na is located in the vicinity of the negatively charged carboxylate groups of oleate ligands or that the Na oleate remains in the final product, for instance with the hydrophobic carbon chain interpenetrated with another oleate molecule bonded to a nanocrystal. Both explanations are consistent with our XRD observation that the structure of the Gd₂O₂S nanocrystals is unchanged with respect to that previously reported.^{6,8} These new results are not compatible with the model of Na-substituted nanoparticles proposed by Ding *et al.* Hereafter, we then attempt to revisit this model by analyzing systematically the role played by different alkali ions on the synthesis of Ln₂O₂S nanoparticles.

2.2 Influence of the nature of alkali ion

The first series of experiments compared the influence of Na oleate and Li acetylacetonate on the reaction yield and on the nanoparticles crystallinity for small lanthanides ions with $Z \geq 64$ (starting from Gd). The choice of the alkali acetylacetonate or oleate complex has no significant influence on the $\text{Ln}_2\text{O}_2\text{S}$ nanoparticles synthesis because oleic acid in the reaction medium substitutes the acetylacetonate ligands. Besides, both acetate and acetylacetonate complexes can be used for the lanthanide precursor. For $\text{Ln} = \text{Sc}$ and Lu , the acetylacetonate complex was not commercially available and the acetate complex was used instead. One should note that short-chained carboxylate were found to affect the overall symmetry and the growth direction of CdSe zinc-blende and cubic FeS_2 nanocrystals.⁹ However, as the $\text{Ln}_2\text{O}_2\text{S}$ already shows a two-dimensional layered structure, and as the oleates are present in all cases in excess, this slight difference in precursor is expected to have only a marginal impact on the present study.

According to Ding *et al.*, Li should be more suitable than Na for substitutions with lanthanides due to the smaller ionic radius (Figure S1). Therefore, we performed a series of experiments, following this assumption. Gd, Dy, Er, Yb, Lu and Sc precursors were employed in a protocol similar to those used to prepare $\text{Gd}_2\text{O}_2\text{S}$. In the case of Yb, Lu and Sc, only Li was tested because the Na^+ radius is at least 0.2 Å larger than that of lanthanide cations.

The reaction yields were all calculated assuming that the $\text{Ln}_2\text{O}_2\text{S}$ phase is formed and that 30 % of the final powder is composed of oleates, as suggested by a previous thermogravimetric analysis combined with mass spectrometry.⁷ For the reactions with $\text{Gd}(\text{acac})_3$ and $\text{Er}(\text{acac})_3$, both Li and Na complexes yielded a significant amount of powder ($\eta \approx 55$ % for Er and $\eta = 60 - 90$ % for Gd). Interestingly, in the case of Er, a first difference was noticed in the color of the final reaction medium, which usually is orange for Gd with $\text{Na}(\text{oleate})$ and pinkish with $\text{Li}(\text{acac})$. $\text{Yb}(\text{acac})_3$ and $\text{Lu}(\text{OAc})_3$ reactions with Li yielded *ca.*

100 mg of powder ($\eta \approx 70\%$). Finally, the reactions of $\text{Sc}(\text{acac})_3$ with Li and $\text{Dy}(\text{acac})_3$ with both alkali ions yielded very small amounts of powder ($\eta < 5\%$).

The powder XRD patterns of some representative samples are presented in Figure 2. In the case of Gd, the XRD peaks are slightly sharper for the sample prepared with Li (Figure 2A). For Dy, the analysis of the patterns is difficult due to the low crystallinity of the powder. The reaction with Na oleate seemingly produced a mixture of $\text{Dy}_2\text{O}_2\text{S}$ and Dy_2O_3 (Figure 2B). However, the reaction yield was low ($\eta < 5\%$), which prevented any further analysis. For Er, the effect of the alkali nature is striking: Na(oleate) led to the formation of another phase, tentatively attributed to erbium oxide whereas Li(acac) yielded erbium oxysulfide (Figure 2C). The analysis of the powder obtained from $\text{Lu}(\text{OAc})_3$ suggests the formation of a mixture of the oxide and of the oxysulfide (Figure 2D).

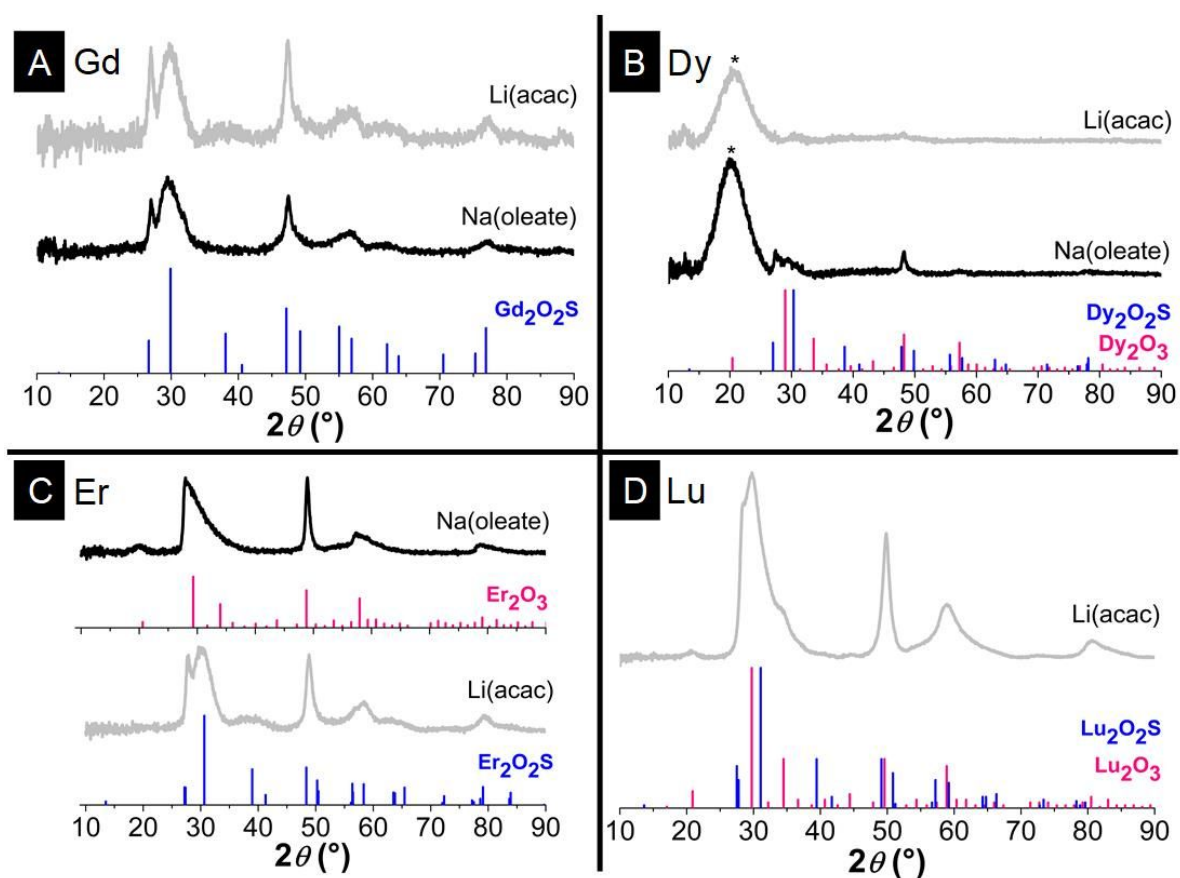


Figure 2: Powder XRD patterns of lanthanide-based nanoparticles; the alkali ion source is indicated on each pattern. Gd (A), Dy (B), Er (C) and Lu (D) oxysulfide nanoparticles were

targeted. Stars indicate the contribution of the plastic dome used to maintain the nanoparticles under inert atmosphere. XRD patterns used as standard are as follows: JCPDS files 26-1422 ($\text{Gd}_2\text{O}_2\text{S}$), 26-0592 ($\text{Dy}_2\text{O}_2\text{S}$), 22-0612 (Dy_2O_3), 65-3445 ($\text{Er}_2\text{O}_2\text{S}$), 08-0050 (Er_2O_3), 26-1445 ($\text{Lu}_2\text{O}_2\text{S}$), 12-0728 (Lu_2O_3).

In Figure 3, we summarize the results of these experiments and compare them with previous reports. In the case of Na, these reports may still be consistent with the substitution model proposed by Ding *et al.* because the reaction occurs only in the presence of sufficiently large lanthanide cations ($Z \leq 65$). This is not the case of Li and K, for the use of Li (K) additives enables the formation of crystalline La (Yb) oxysulfide nanoparticles (Figure 3, mark **a,c**).

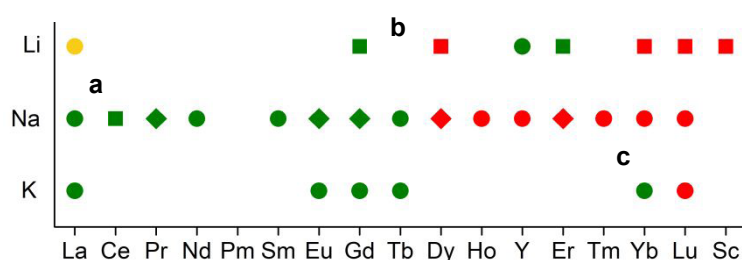


Figure 3: Influence of the alkali nature on the crystallization of $\text{Ln}_2\text{O}_2\text{S}$ and $\text{Y}_2\text{O}_2\text{S}$ nanoparticles from Ding *et al.*⁴ or Zhang *et al.*⁵ (circles), our work (squares) and both works (diamonds). On both axes, cations are ordered as a function of decreasing radius size. Color codes are as follows: crystalline oxysulfide nanoparticles (green); poorly crystallized nanoparticles (yellow); no nanoparticles, oxide nanoparticles or mixture (red).

Some results are intriguing. For instance, crystalline Gd, Y and Er oxysulfide nanoparticles were obtained using Li. The contrary was found in the case of Dy, whose cation radius is comprised between Gd and Y (Figure 3, mark **b**). In view of the above, we should conclude that the substitution model is unlikely, though no consistent picture could be proposed.

2.3 Influence of the alkali stoichiometry

In the works of Ding *et al.*⁴ and Zhang *et al.*,⁵ the alkali stoichiometry was maintained at 1 equiv. *vs.* the lanthanide for all the syntheses. In 2013, Gu *et al.* crystallized Ln₂O₂S nanoplates without alkali using gaseous H₂S as sulfidating agent, though this is not a colloidal process.¹⁰ More recently, in 2017, Lei *et al.* successfully obtained crystalline Gd₂O₂S nanoparticles without alkali source with a modified procedure involving a large excess of elemental sulfur (20 equiv. *vs.* Gd).¹¹ The authors tested Na and Y substitutions under these conditions and found that the nanoparticle size increases with increasing Na concentration (0 equiv.; 1 equiv.; 4 equiv. *vs.* Gd) and that Y affects the final morphology. According to the authors, the presence of the alkali ion is not mandatory but seems to largely favor the crystallization process.

Here, we performed the reaction using a stoichiometric amount of S in the absence of Na and obtained an amorphous product composed of ~3 nm-sized objects with a yield below 5 % (Figure 4A and F). We then reproduced the synthesis route described by Lei *et al.*¹¹ without Na in an excess of S (20 equiv. S *vs.* Gd, 315 °C, 1 h) and produced only a few milligrams of solid. This is much lower than the 100 mg expected for a quantitative yield, despite having optimized the solvent mixture for the washing procedure. In order to explain these results, we propose that either Na is necessary for the crystallization of the nanoplates, as suggested by Ding and Zhang, or that the crystallization is kinetically enhanced by the alkali complex.

To investigate the role of Na in the crystallization process of Gd₂O₂S nanoplates in the case of stoichiometric sulfur composition, we carried out the reaction with various Na stoichiometries. It is recalled that, using a concentration of 1 equiv. *vs.* Gd, we obtained 7 nm-wide crystalline nanoplates, while a 0 equiv. *vs.* Gd stoichiometry yielded low amount of small amorphous nanoparticles.⁶

Surprising is the observation that crystalline $\text{Gd}_2\text{O}_2\text{S}$ nanoparticles were formed using a low Na concentration (see Table S1 and Figure 4). 0.01 equiv. of sodium yielded small nanoplates but the EDS S:Gd composition was only 0.06 (Table S1). Accordingly, the XRD pattern showed a broad peak in the $25\text{-}35^\circ$ range indicating the possible presence of Gd oxide nanoparticles (although a final attribution cannot be made at this point) and probably a small amount of Gd oxysulfide nanoparticles (Figure 4F). With 0.50 equiv., the nanoparticles were well crystallized and similar to the sample prepared using 1.00 equiv., even if the aggregation of the nanoplates was less pronounced (Figure 4D and F). At 0.10 equiv., the XRD pattern already shows the formation of a pure oxysulfide phase even if the crystallinity was poorer as compared to the samples obtained by using higher Na concentrations (Figure 4F indicates broader peaks on top of an even broader signal attributed to an amorphous component). Interestingly, the Na amount in the isolated powder was decreased to about 0.05 equiv. *vs.* Gd for nominal Na:Gd ratio of 0.10 and 0.50 (Table S1). We came to the conclusion that washing is unable to completely remove the remaining sodium. This is consistent with the hypothesis that Na cations are trapped around the carboxylate groups of oleate ligands so that a minimum amount of sodium remains on the final nanoparticles. A key result is that only 0.10 equiv. of Na is both necessary and sufficient to crystallize the oxysulfide. In order to understand the cation role, the formation of the colloids was analyzed using X-ray scattering in the small and wide-angle domains (SAXS-WAXS).

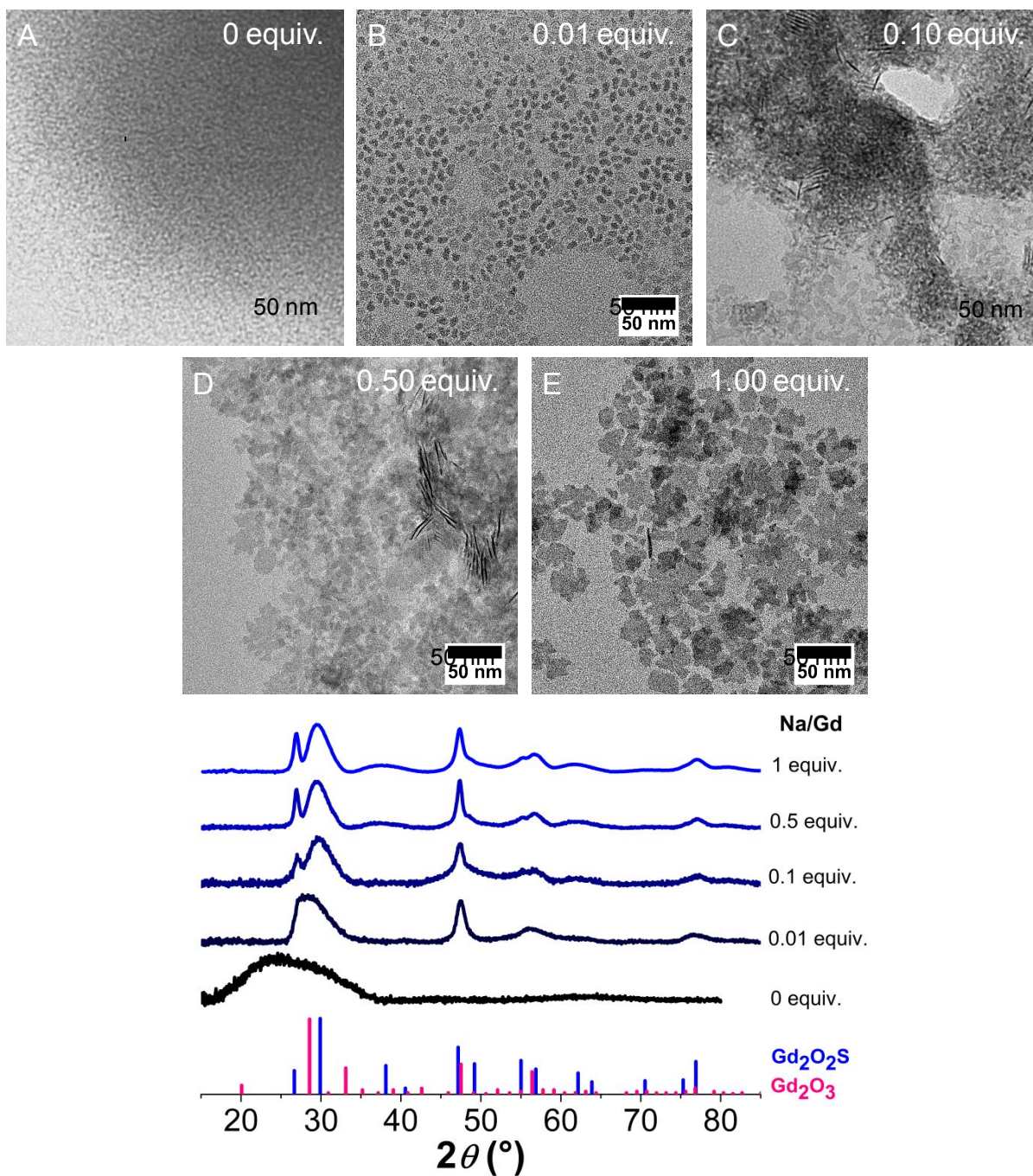


Figure 4: Effect of Na oleate stoichiometry in the crystallization of Gd_2O_2S nanoparticles. TEM micrographs on final particles obtained with 0 (A), 0.01 (B), 0.50 (C) and 1.00 equiv. of Na(oleate) vs. $Gd(acac)_3$ and their corresponding powder XRD patterns (E).

2.4 Nucleation and growth of Gd_2O_2S nanoparticles from SAXS-WAXS

Previous reports on $\text{Ln}_2\text{O}_2\text{S}$ nanoparticles do not address the issue of the formation mechanisms in either aqueous or organic media. The first step in water-based syntheses, which is the formation of the so-called “oxygenated precursor” (hydroxycarbonate, oxide, hydroxide...) is poorly described by lack of characterization of the intermediates before sulfidation. In addition, the mechanism of the sulfidation step, generally performed by solid-solid or solid-gas reaction with a large excess of H_2S ,¹² S_8 ^{13–15} or *in situ* produced CS_2 ,^{16,17} has not been studied yet despite the thermodynamic cost of substituting oxide anions with sulfide ones. In organic media, the discussions on the mechanism of $\text{Ln}_2\text{O}_2\text{S}$ formation are found in the articles of Ding *et al.* and their successors.^{4,10,11} They were not supported by experimental data obtained during the synthesis, but rather by an in-depth analysis of the products.

For the present study, we carried out an *in situ* small- and wide-angle X-ray scattering (SAXS and WAXS), suitable to probe aliquots taken on site from the reaction flask during the synthesis of the $\text{Gd}_2\text{O}_2\text{S}$ nanoplates. SAXS-WAXS were successfully used in the past to clarify nucleation and growth of nanoparticles in colloidal solution.^{18,19,20} Here, a preliminary experiment on colloidal solutions of the final states of syntheses with 1 equiv. of sodium showed that the solutions aged over a few days (Figure S3). This aging phenomenon is interesting but out the scope of the present study. In order to perform SAXS-WAXS, aliquots of the as-prepared solution were taken from the reaction flask then quickly cooled down to r.t. and finally inserted in a capillary. This methodology provides an unavoidable time delay that was shortened by performing the synthesis on the room adjacent to the SAXS apparatus.

2.4.1 Final state of the synthesis

The SAXS-WAXS patterns, taken after the reaction is complete, indicate a two-level aggregation (Figure 5): (i) aggregates of stacked and free $\text{Gd}_2\text{O}_2\text{S}$ nanoplates; (ii) these aggregates are themselves assembled into larger objects, in agreement with TEM observations

(Figure 6A). We analyzed the patterns using a model of this two-level aggregation of stacked and free circular nanoplates (see Supporting Information) by assigning the broad correlation signal at $q \approx 10^{-1} \text{ \AA}^{-1}$ to the constituting nanometer-sized $\text{Gd}_2\text{O}_2\text{S}$ nanoplates of 4.7 nm diameter and 0.9 nm thickness (Figure 6C). The correlation signal is superimposed to the series of $(00k)$ Bragg peaks with spacing $\Delta q = 0.14 \text{ \AA}^{-1}$, indicating that stacks of lamellas have a spacing of 4.5 nm (Figure 6B). Both the width of the Bragg peaks and the correlation signal at $q \approx 10^{-2} \text{ \AA}^{-1}$ and their relative intensities indicate that, in average, the aggregates are made of stacks of 5.3 lamellas and of 5.7 non-stacked lamellas (Figure 6B). Finally, the aggregates are assembled into even larger structures, as evidenced by the power-law decay at small angles. The slope of the decay indicates that the larger structures are mass fractal aggregates with fractal dimension $D = 2.1$, indicative of porous structures.²¹

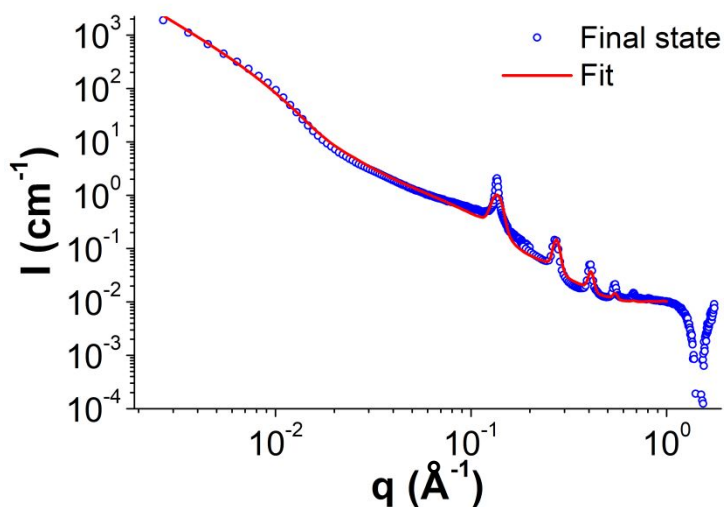


Figure 5: Blue open circles are SAXS-WAXS data for the final state of the $\text{Gd}_2\text{O}_2\text{S}$ nanoparticles obtained with 1.00 equiv. of $\text{Na}(\text{oleate})$ vs. $\text{Gd}(\text{acac})_3$. The solid red line is a best fit using a model of mixed free and aggregated nanoplates (see Supplementary Information).

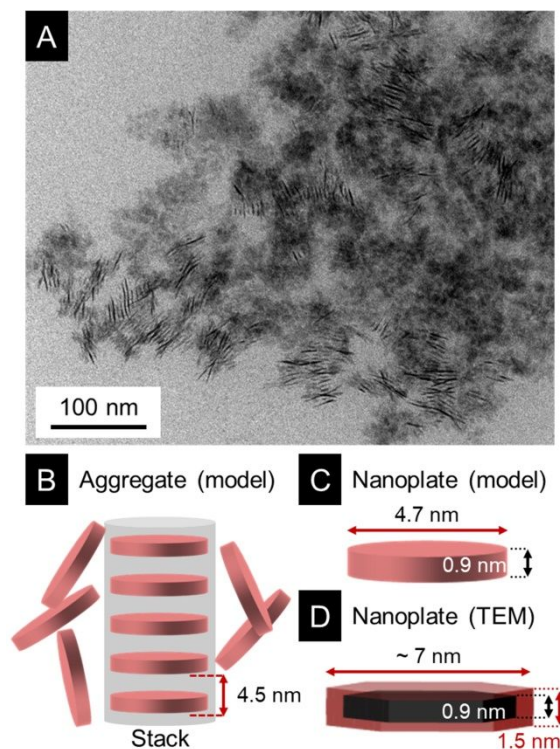


Figure 6: (A) Typical aggregates of Gd_2O_2S nanoplates observed by TEM. (B) Model aggregate composed of stack and disordered nanoplates derived from the SAXS-WAXS results. (C) Geometric model of individual nanoplate derived from the SAXS-WAXS results. (D) Model of Gd_2O_2S nanoplates derived from the present TEM study and from previous work.^{6,8}

The model proposed to describe the final powder correctly accounts for the presence of stacks in the powder. For the smaller building block, *i.e.* the nanoplate, the model (Figure 6C) converges to the correct aspect ratio of 0.2 (thickness over diameter) but the absolute values are smaller than those expected from the TEM observation (Figure 6D). In order to explain this discrepancy, we propose that the outer layer of the nanoparticles (in red in Figure 6D), strongly bonded to oleate ligands⁷ and partially disordered due to partial oxidation,⁶ produces a modest X-ray contrast with the outer medium.

Overall, the analysis of the SAXS-WAXS data obtained on the final state powders agrees with our previous observations and provides a more accurate description of the aggregates. In particular, it provides a set of parameters to interpret aliquots taken during the synthesis.

These parameters will be exploited below to explain the structuring role of the solvent during the formation of the nanoparticles, by following aliquots taken during the synthesis.

2.4.2 From complexes to nuclei

Aliquots were taken at selected temperatures during three synthesis steps after the 120 °C dwell for degassing, during the heating ramp and during the 310 °C dwell. These aliquots were analyzed in two series below and above 300 °C.

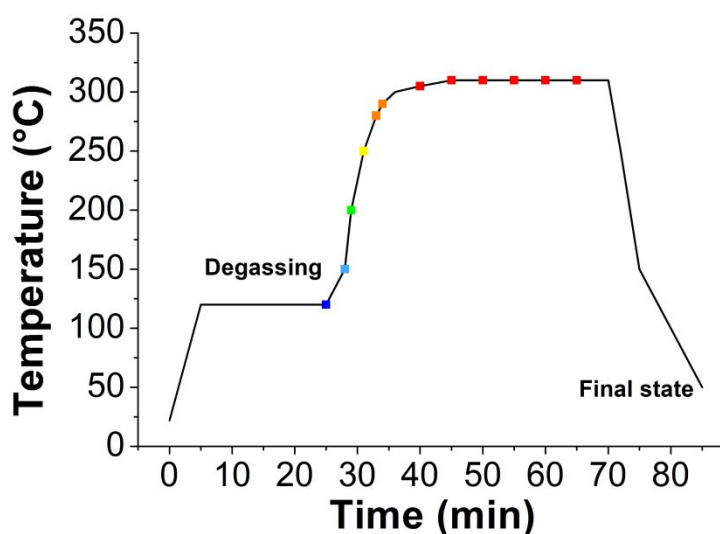


Figure 7: Aliquots analyzed by SAXS-WAXS.

Below 300 °C, the SAXS-WAXS (Figure 8, Figure S5) curves are distinct from the final state (Figure 5). At the early stages of the reaction, the form factor of the Gd_2O_2S nanoplates is not observed yet. We observe cylinders stacked into an inverse hexagonal phase, themselves aggregated into larger structures. The cylindrical shape is evident from the form factor characterized by a broad correlation signal decaying as $I \propto q^{-1}$ in between $3 \cdot 10^{-2}$ and 1 \AA^{-1} . The cylinders are assigned to inverse micelles with an inorganic core, surrounded by amphiphilic ligands, with a diameter of 0.5 nm and a length of 4.7 nm. The ordered stacking of cylinders into an inverse hexagonal phase is evident from the superstructure peaks above $q = 0.06 \text{ \AA}^{-1}$. As in the final state, we already observe the Bragg peaks of a lamellar stacking with a spacing of 4.3 nm ($q = 0.14 \text{ \AA}^{-1}$, 0.28 \AA^{-1} and 0.42 \AA^{-1} , Figure 8). Contrary to the final

state, the model for the lamellar phase alone is unable to properly describe the signal. Instead, we found additional contributions of the inverse hexagonal phase (Figure 8 and Figure S5) as a series of Bragg peaks, with $\frac{4\pi k}{a\sqrt{3}}$ spacing, where $k = 1, \sqrt{3}, \sqrt{4}$ and $a = 8.6$ nm is the distance between cores of adjacent cylinders.²² Consistent with a possible hexagonal-to-lamellar transition as the chemical reaction proceeds, the lamellar and inverse hexagonal phases are commensurate, *i.e.* the (001) distance of the lamellar phase coincides with the 11 distance of the 2D hexagonal phase. The aggregates are assembled into even larger structures, as indicated by the power-law decay at small angles. The slope of the decay indicates that the larger structures are surface fractal aggregates with a fractal dimension $D = 2.7$, indicative of dense structures.²³

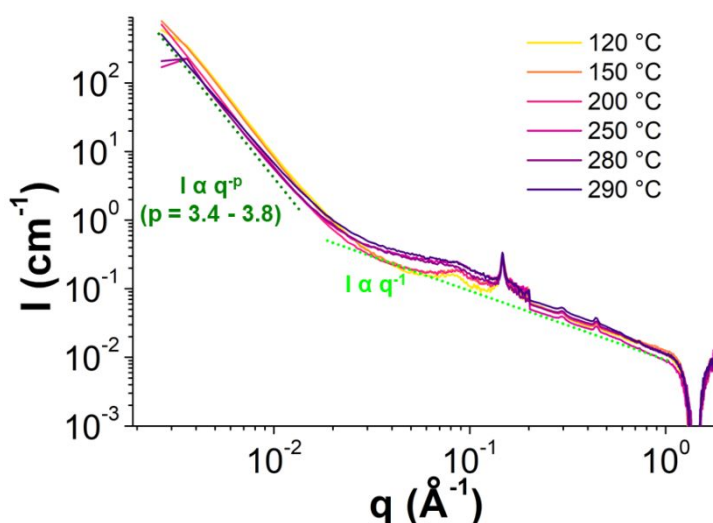


Figure 8: SAXS-WAXS obtained from samples taken during the heating ramp. The SAXS and WAXS data were merged at 0.20 \AA^{-1} . Dotted lines are a guide to the eye. This figure is redrawn in a larger version as Figure S8.

Interestingly, the lamellar phase and the correlation signal are already observable at $120 \text{ }^\circ\text{C}$ (Figure S5). It indicates that at the earliest stage of the synthesis, the solvent and/or the complexes are already structured. This contrasts with the case of the pristine solvent, where

no structure is observable at ambient temperature from the SAXS-WAXS pattern (Figure S4). We conclude that the cations participate in the formation of both the initial inverse hexagonal structure and the lamellar structure (Figure 9). This conclusion is consistent with the literature, where it is reported that oleic acid is an isotropic liquid in the 15 - 130 °C range.²⁴ Moreover, in a oleic acid/Na(oleates) mixture, all the oleic acid is liquid above 32 °C but a fraction of Na(oleates) remains solid-like with a lamellar organization, with a characteristic spacing of 4.5 nm.²⁴

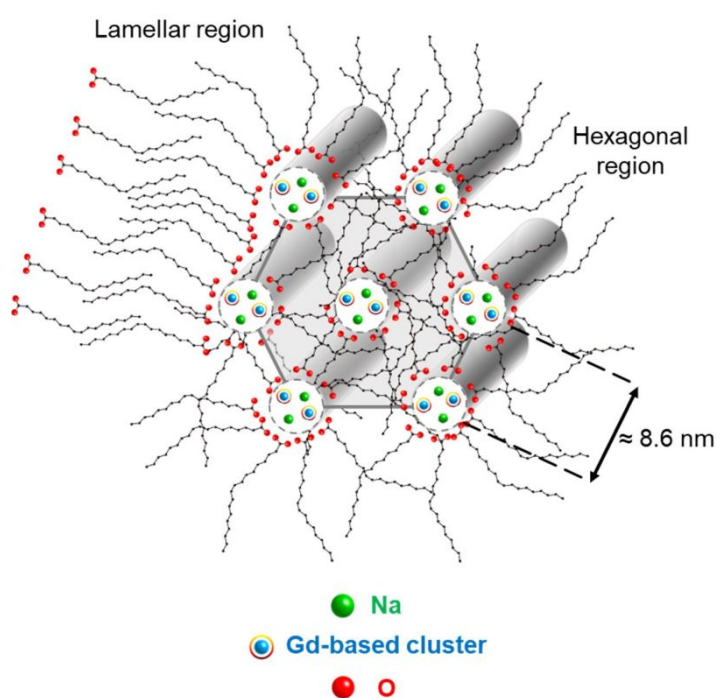


Figure 9: Proposed organization of the mixed inverse hexagonal and lamellar phases in the 120 - 200 °C range, following Rappolt *et al.*²²

At 200 °C, a first change occurs. The correlation signal at $q = 8.10^{-2} \text{ \AA}^{-1}$, assigned to the first superstructure peak of the inverse hexagonal phase, starts to fade and vanishes at 310 °C. This modification is assigned to the destruction of the inverse hexagonal phase. In parallel, the first step of the nucleation occurs, during which the clusters form small 1.5 nm-sized objects. The formation of the nanoplates decreases the curvature of the micelles, driving the

transition from the inverse hexagonal phase to the lamellar phase. The width of these nuclei is limited and we find no sign yet of the aggregates in the final state which contains stacks, as seen in Figure 6.

2.4.3 Nanoparticles growth

Above 290 °C, the X-ray scattering profiles are changed significantly. At 310 °C, the nanoplates are formed, as confirmed by the TEM results shown in Figures S6 and S7, and all the features characterizing the final state are found (see Figure 10). The increase of the low- q intensity with temperature indicates an increase of the crystalline fraction, consistent with the fact that more and more nanoplates are formed. At higher q values, the characteristic peaks of the lamellar structure become increasingly distinct and slightly shifted towards small angles.

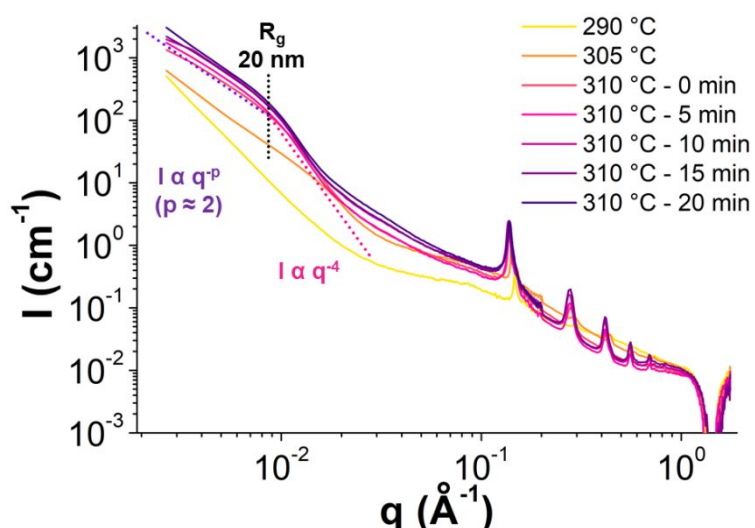


Figure 10: SAXS-WAXS obtained above 300 °C. The SAXS and WAXS data were merged at 0.20 \AA^{-1} , which explains the small step in the intensity. Dotted lines are a guide to the eye. This figure is redrawn in a larger version as Figure S9.

At 305 °C, the nuclei begin to assemble, though the nanoplate size is still smaller than the final one. An increased intensity in the low- q region and an inflection point around $2 \cdot 10^{-2} \text{ \AA}^{-1}$, indicating a lower gyration radius than in the final state, reflects the formation of the aggregates. Both the growth and the aggregation of the nanoplates are completed during the 310 °C dwell, for the corresponding SAXS/WAXS pattern coincides with that of the final

particles. The mechanism of nanoparticle formation is schematically illustrated in Figure 11. It illustrates the nucleation of the lanthanide oxysulfide crystal in the *ca.* 1.5 nm-wide interlayer space of the lamellar phase.

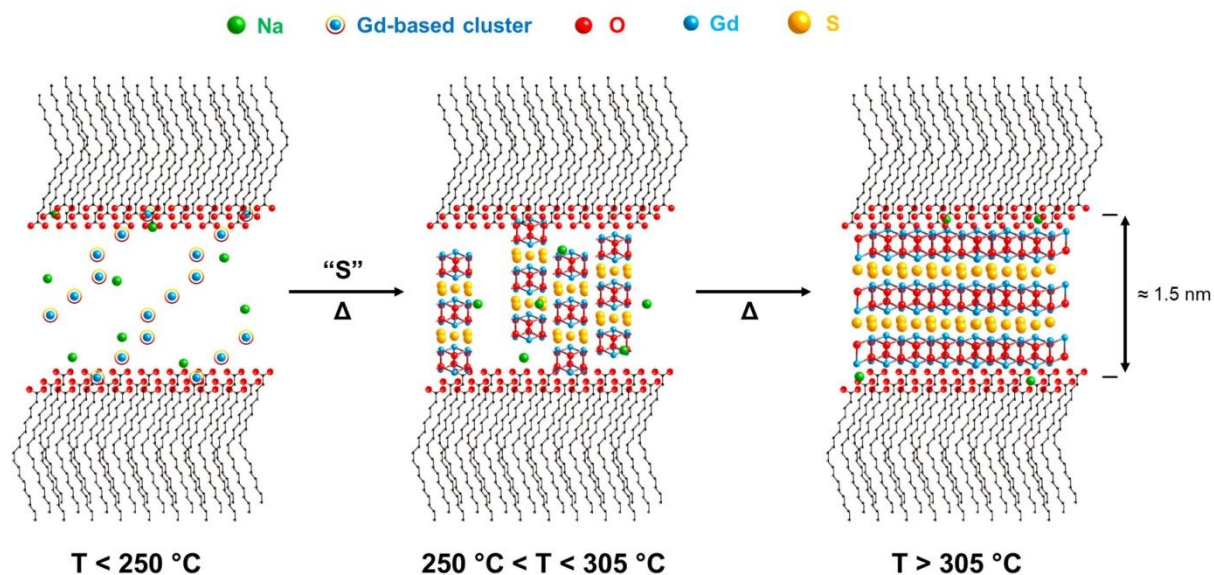


Figure 11: Proposed mechanism of $\text{Gd}_2\text{O}_2\text{S}$ nanoparticle formation starting from organized clusters.

3. Conclusion

In the present study, we investigated the role of the alkali cation in the colloidal synthesis of $\text{Ln}_2\text{O}_2\text{S}$ nanoparticles in organic solvents. We first put into question the current proposal of partial substitution of the lanthanide by Na by giving experimental evidence that Na is weakly bound to the surface and that its removal does not affect the lattice parameter of the nanoparticles. Second, by using smaller and larger alkali cations (Li and K, respectively) for the synthesis of a series of oxysulfides of Ln and of Y, we showed that the above substitution is unlikely due to large difference in cation size and to the lack of a consistent trend in the properties of nanoparticles synthesized using systematically various metals and alkali cations.

We then attempted to establish an alternative model of nanoparticle formation by considering Na and Gd for our case study. We demonstrated that 0.10 equiv. of Na *vs.* Gd is

enough to obtain well-crystallized $\text{Gd}_2\text{O}_2\text{S}$ nanoparticles. In order to identify the role of Na on the crystallization process, we analyzed SAXS-WAXS aliquots of the colloidal synthesis taken at various times and temperature during synthesis. The SAXS results put into evidence that a lamellar mesophase, consistent with a bilayer structure of sodium oleate, is formed at the early stage of the reaction (120 °C) and persists up to high temperatures (310 °C). We observed that the nucleation of the nanoparticles starts at 250 °C, suggesting that this initial stage takes place within the mesophase. The final crystallization of the nanoplates in the $\text{Gd}_2\text{O}_2\text{S}$ structure occurs at 305 °C and the growth of the nanoplates develops during the heating dwell at 310 °C. As a perspective, *in situ* SAXS measurements performed with synchrotron light might provide additional details on the kinetics of these processes.

Overall, the above mechanism explains why a substoichiometric amount of Na is sufficient to form the $\text{Gd}_2\text{O}_2\text{S}$ structure. Namely, the Na concentration within the oleate-rich solvent mixture and not its stoichiometry is relevant to the formation process. The proposed mesophase mechanism reconciles previous and present results reported on the synthesis and characterization of $\text{Ln}_2\text{O}_2\text{S}$ nanoparticles. Since oleates are commonly employed as surfactants, a similar mechanism might be relevant to a wide range of other colloidal syntheses. Moreover, a similar method could usefully be applied to the case of Li and K alkalis in order to verify that a similar mesophase is at stake in these cases.

4. Experimental section

4.1 Nanoparticles synthesis

Monometallic and bimetallic oxysulfides nanoparticles were prepared *via* a solvothermal reaction including a mixture of organic solvents and metallic complexes. Oleylamine (OM; technical grade, 70 %), oleic acid (OA; technical grade, 90 %), sulfur (S_8 ; ≥ 99.5 %) and sodium oleate ($\text{Na}(\text{oleate})$; ≥ 99 %) were purchased from Sigma-Aldrich. 1-octadecene (ODE;

technical grade, 90 %) was purchased from Acros Organics. Gadolinium acetylacetonate hydrate ($\text{Gd}(\text{acac})_3 \cdot x\text{H}_2\text{O}$; 99.9 %) and cerium acetylacetonate hydrate ($\text{Ce}(\text{acac})_3 \cdot x\text{H}_2\text{O}$; 99.9 %) were purchased from Strem Chemicals. All products were used as received without further purification.

In a typical synthesis of $\text{Ln}_2\text{O}_2\text{S}$, $\text{Ln}(\text{acac})_3 \cdot x\text{H}_2\text{O}$ (0.50 mmol), S_8 (0.032 mmol), $\text{Na}(\text{oleate})$ or $\text{Li}(\text{acac})$ (0.50 mmol), OM (17 mmol), OA (2.5 mmol) and ODE (32.5 mmol) were added in a 100 mL three-neck flask at room temperature. For $\text{Ln} = \text{Sc}$ and Lu , $\text{Ln}(\text{ac})_3 \cdot x\text{H}_2\text{O}$ was used instead of $\text{Ln}(\text{acac})_3 \cdot x\text{H}_2\text{O}$. The solution was heated to 120 °C under vacuum for 20 minutes to remove water and other impurities with low boiling points. The mixture was then heated to 310 °C and stirred at this temperature for 30 minutes under purified N_2 . The transparent solution gradually became turbid starting from 280 °C. Then the mixture was left to cool to room temperature under N_2 . The nanoparticles were isolated using ethanol and washed at least three times using a THF/ethanol (1/5) mixture to remove the remaining reagents and organic matter.

For $\text{Gd}_{2(1-y)}\text{Ce}_{2y}\text{O}_2\text{S}$ nanoparticles bimetallic nanoparticles, the protocol is similar with $\text{Gd}(\text{acac})_3 \cdot x\text{H}_2\text{O}$ and $\text{Ce}(\text{acac})_3 \cdot x\text{H}_2\text{O}$ (0.50 mmol) as starting organometallic reagents. A 40 to 90 mg amount of dried $\text{Gd}_{2(1-y)}\text{Ce}_{2y}\text{O}_2\text{S}$ nanoparticles was thus obtained depending on the initial cerium loading.

4.2 Nanoparticles characterization

TEM: A drop of a diluted solution of $\text{Gd}_{2(1-y)}\text{Ce}_{2y}\text{O}_2\text{S}$ dispersed in pure THF was allowed to dry on an amorphous carbon-coated copper grid. TEM images were collected with a TWIN 120 (TECNAI SPIRIT) at 120 kV and with a JEOL 100CF.

XRD: The X-ray diffraction patterns of dry powders were measured on a Bruker D8 diffractometer using $\text{Cu K}\alpha$ radiation at 1.5406 Å. Typical diffractograms were collected with

steps of 0.05° and a scanning speed of 5 s/point. The backgrounds of the patterns were subtracted using the EVA software.

EDS on the SEM: A small amount of powder was deposited on a carbon adhesive tape on a scanning electron microscope sample holder. A layer of carbon was deposited on the samples for electronic conductivity. EDS analyses were performed on a SEM HITACHI S-3400N at 10 kV. Titanium was chosen as reference and analyses were performed on three to five different zones on each sample.

4.3 SAXS-WAXS measurements and data treatment process

For the SAXS-WAXS experiments, the reaction medium was sampled at different temperatures. The reaction was never interrupted to prevent modifications of the reaction time. To take an aliquot, the flow of inert gas was turned off and the sample was swiftly taken off by a Pasteur pipette. The total sampled amount did not exceed half of the reaction medium (around 0.4 mL / sample, total volume of 16 mL) to maintain the same reaction dynamics in the flask. The hot sample is immediately cooled down by a water bath at ambient temperature under inert atmosphere. Because of the small volume of the sample, only a few seconds are necessary to cool the sample down to temperatures close to room temperature. The sample was then placed in the capillary, which was hermetically sealed because the analysis chamber is under vacuum.

Apparatus and measurement conditions: Small- and wide-angle X-ray scattering (SAXS/WAXS) measurements were performed with a commercial setup (Xeuss 2.0, Xenocs) at a wavelength of $\lambda = 1.54 \text{ \AA}$ using two complementary sample-to-detector distances to span wavevector ranges of $2.7 \cdot 10^{-3} \text{ \AA}^{-1} \leq q \leq 2.6 \cdot 10^{-3} \text{ \AA}^{-1}$ (SAXS) and $9.6 \cdot 10^{-2} \text{ \AA}^{-1} \leq q \leq 1.75 \text{ \AA}^{-1}$ (WAXS).

The sample–detector distance was calibrated with tetradecanol. The detector count was normalized to differential cross-sections per volume with Lupolen as a secondary reference ($I_{max} = 6 \text{ cm}^{-1}$), and with a photon count across the sample as a monitor or the direct beam. Samples were contained in sealed glass capillaries with a 1.2 mm optical path, as determined by the scattering intensity of water ($1.6 \cdot 10^{-2} \text{ cm}^{-1}$), and measured under vacuum. Data analysis and fitting parameters are detailed in the Supporting Information.

5. Acknowledgements

This work was supported by the French ANR within the Investissements d'Avenir programme under reference ANR-11-IDEX-0004-02, and specifically within the framework of the Cluster of Excellence MATISSE led by Sorbonne Université. Partial support was provided by the ANR project OxySUN (ANR-16-CE09-0005) through the funding of the PhD thesis of TKCL and by the ANR project DIAMONS (ANR-14-CE08-0003). The doctoral Program IPV of Sorbonne Université is acknowledged for funding the PhD thesis of AMN. Sorbonne Université, CNRS, and the Collège de France are acknowledged for financial support. We are especially grateful to Jean-Claude Berthet and Thibault Cantat at CEA Saclay for their assistance and a Schlenk line onsite for preparing the SAXS-WAXS aliquots.

6. Supporting information available

Supporting information available: ionic radii of selected cations, complementary data from XRD, EDS and TEM, $\text{Gd}_2\text{O}_2\text{S}$ crystal structure, SAXS-WAXS experimental data and data modeling. This material is available free of charge via the internet at <http://pubs.acs.org>.

7. References

- (1) Li, Y.; Huang, Y.; Bai, T.; Li, L. Straightforward Conversion Route to Nanocrystalline Monothiooxides of Rare Earths through a High-Temperature Colloid Technique. *Inorg. Chem.* **2000**, *39* (15), 3418–3420.

- (2) Ajithkumar, G.; Yoo, B.; Goral, D. E.; Hornsby, P. J.; Lin, A.-L.; Ladiwala, U.; Dravid, V. P.; Sardar, D. K. Multimodal Bioimaging Using a Rare Earth Doped $\text{Gd}_2\text{O}_2\text{S}:\text{Yb}/\text{Er}$ Phosphor with Upconversion Luminescence and Magnetic Resonance Properties. *J. Mater. Chem. B* **2013**, *1* (11), 1561.
- (3) Rosticher, C.; Viana, B.; Fortin, M.-A.; Lagueux, J.; Faucher, L.; Chanéac, C. Gadolinium Oxysulfide Nanoprobes with Both Persistent Luminescent and Magnetic Properties for Multimodal Imaging. *RSC Adv.* **2016**, *6* (60), 55472–55478.
- (4) Ding, Y.; Gu, J.; Ke, J.; Zhang, Y.-W.; Yan, C.-H. Sodium Doping Controlled Synthesis of Monodisperse Lanthanide Oxysulfide Ultrathin Nanoplates Guided by Density Functional Calculations. *Angew. Chemie Int. Ed.* **2011**, *50* (51), 12330–12334.
- (5) Zhang, T.; Gu, J.; Ding, Y.; Zhang, Y.-W.; Yan, C.-H. Experimental and Theoretical Studies on the Controlled Synthesis of Alkali-Metal-Doped Rare-Earth Oxysulfide Nanocrystals. *Chempluschem* **2013**, *78* (6), 515–521.
- (6) Larquet, C.; Nguyen, A.-M.; Ávila-Gutiérrez, M.; Tinat, L.; Lassalle-Kaiser, B.; Gallet, J.-J.; Bournel, F.; Gauzzi, A.; Sanchez, C.; Carenco, S. Synthesis of $\text{Ce}_2\text{O}_2\text{S}$ and $\text{Gd}_{2(1-y)}\text{Ce}_y\text{O}_2\text{S}$ Nanoparticles and Reactivity from in Situ X-Ray Absorption Spectroscopy and X-Ray Photoelectron Spectroscopy. *Inorg. Chem.* **2017**, *56* (22), 14227–14236.
- (7) Larquet, C.; Hourlier, D.; Nguyen, A.-M.; Torres-Pardo, A.; Gauzzi, A.; Sanchez, C.; Carenco, S. Thermal Stability of Oleate-Stabilized $\text{Gd}_2\text{O}_2\text{S}$ Nanoplates in Inert and Oxidizing Atmospheres. *ChemNanoMat* **2019**, *5* (4), 539–546.
- (8) Larquet, C.; Nguyen, A.-M.; Glais, E.; Paulatto, L.; Sassoie, C.; Selmane, M.; Lecante, P.; Maheu, C.; Geantet, C.; Cardenas, L.; et al. Band Gap Engineering from Cation Balance: The Case of Lanthanide Oxysulfide Nanoparticles. *Chem. Mater.* **2019**, *31* (14), 5014–5023.
- (9) Riedinger, A.; Ott, F. D.; Mule, A.; Mazzotti, S.; Knüsel, P. N.; Kress, S. J. P.; Prins,

- F.; Erwin, S. C.; Norris, D. J. An Intrinsic Growth Instability in Isotropic Materials Leads to Quasi-Two-Dimensional Nanoplatelets. *Nat. Mater.* **2017**, *16* (7), 743–748.
- (10) Gu, J.; Ding, Y.; Ke, J.; Zhang, Y.; Yan, C. Controllable Synthesis of Monodispersed Middle and Heavy Rare Earth Oxysulfide Nanoplates Based on the Principles of HSAB Theory. *Acta Chim. Sin.* **2013**, *71* (3), 360.
- (11) Lei, L.; Zhang, S.; Xia, H.; Tian, Y.; Zhang, J.; Xu, S. Controlled Synthesis of Lanthanide-Doped Gd₂O₂S Nanocrystals with Novel Excitation-Dependent Multicolor Emissions. *Nanoscale* **2017**, *9* (17), 5718–5724.
- (12) Osseni, S. A.; Lechevallier, S.; Verelst, M.; Dujardin, C.; Dexpert-Ghys, J.; Neumeyer, D.; Leclercq, M.; Baaziz, H.; Cussac, D.; Santran, V.; et al. New Nanoplatfrom Based on Gd₂O₂S:Eu³⁺ Core: Synthesis, Characterization and Use for in Vitro Bio-Labeling. *J. Mater. Chem.* **2011**, *21* (45), 18365.
- (13) Song, Y.; You, H.; Huang, Y.; Yang, M.; Zheng, Y.; Zhang, L.; Guo, N. Highly Uniform and Monodisperse Gd₂O₂S:Ln³⁺ (Ln = Eu, Tb) Submicrospheres: Solvothermal Synthesis and Luminescence Properties. *Inorg. Chem.* **2010**, *49* (24), 11499–11504.
- (14) Fu, Y.; Cao, W.; Peng, Y.; Luo, X.; Xing, M. The Upconversion Luminescence Properties of the Yb³⁺–Ho³⁺ System in Nanocrystalline Y₂O₂S. *J. Mater. Sci.* **2010**, *45* (23), 6556–6561.
- (15) Luo, X.; Cao, W.; Xing, M. Upconversion Luminescence Properties of Monodisperse Spherical Y₂O₂S:Yb, Ho Nanocrystals. *J. Mater. Res.* **2009**, *24* (05), 1756–1760.
- (16) Thirumalai, J.; Chandramohan, R.; Divakar, R.; Mohandas, E.; Sekar, M.; Parameswaran, P. Eu³⁺ Doped Gadolinium Oxysulfide (Gd₂O₂S) Nanostructures—Synthesis and Optical and Electronic Properties. *Nanotechnology* **2008**, *19* (39), 395703.

- (17) Han, L.; Hu, Y.; Pan, M.; Xie, Y.; Liu, Y.; Li, D.; Dong, X. A New Tactic to Achieve $\text{Y}_2\text{O}_2\text{S}:\text{Yb}^{3+}/\text{Er}^{3+}$ up-Conversion Luminescent Hollow Nanofibers. *CrystEngComm* **2015**, *17* (12), 2529–2535.
- (18) Abécassis, B.; Testard, F.; Spalla, O.; Barboux, P. Probing in Situ the Nucleation and Growth of Gold Nanoparticles by Small-Angle X-Ray Scattering. *Nano Lett.* **2007**, *7* (6), 1723–1727.
- (19) Cravillon, J.; Schröder, C. A.; Nayuk, R.; Gummel, J.; Huber, K.; Wiebcke, M. Fast Nucleation and Growth of ZIF-8 Nanocrystals Monitored by Time-Resolved In Situ Small-Angle and Wide-Angle X-Ray Scattering. *Angew. Chemie Int. Ed.* **2011**, *50* (35), 8067–8071.
- (20) Fleury, B.; Neouze, M.-A.; Guigner, J.-M.; Menguy, N.; Spalla, O.; Gacoin, T.; Carriere, D. Amorphous to Crystal Conversion as a Mechanism Governing the Structure of Luminescent $\text{YVO}_4:\text{Eu}$ Nanoparticles. *ACS Nano* **2014**, *8* (3), 2602–2608.
- (21) Teixeira, J. Small-Angle Scattering by Fractal Systems. *J. Appl. Crystallogr.* **1988**, *21* (6), 781–785.
- (22) Rappolt, M.; Hickel, A.; Bringezu, F.; Lohner, K. Mechanism of the Lamellar/Inverse Hexagonal Phase Transition Examined by High Resolution X-Ray Diffraction. *Biophys. J.* **2003**, *84* (5), 3111–3122.
- (23) Besselink, R.; Stawski, T. M.; Van Driessche, A. E. S.; Benning, L. G. Not Just Fractal Surfaces, but Surface Fractal Aggregates: Derivation of the Expression for the Structure Factor and Its Applications. *J. Chem. Phys.* **2016**, *145* (21), 211908.
- (24) Tandon, P.; Raudenkolb, S.; Neubert, R. H. .; Rettig, W.; Wartewig, S. X-Ray Diffraction and Spectroscopic Studies of Oleic Acid–Sodium Oleate. *Chem. Phys. Lipids* **2001**, *109* (1), 37–45.